

Preferred Synthesis of Armchair SnS₂ Nanotubes

Abid^{1†}, Luneng Zhao^{2†}, Ju Huang^{3†}, Yongjia Zheng^{1†}, Yuta Sato^{4,5}, Qingyun Lin⁶, Zhen Han⁷, Chunxia Yang¹, Tianyu Wang¹, Bill Herve Nduwarugira¹, Yicheng Ma¹, Lingfeng Wang¹, Yige Zheng¹, Hang Wang¹, Salman Ullah¹, Afzal Khan¹, Qi Zhang⁸, Wenbin Li^{3*}, Junfeng Gao^{2*}, Bingfeng Ju¹, Feng Ding⁹, Yan Li⁷, Kazu Suenaga^{5*}, Shigeo Maruyama¹⁰, Huayong Yang¹, Rong Xiang^{1*}

¹*State Key Laboratory of Fluid Power and Mechatronic Systems, School of Mechanical Engineering, Zhejiang University, Hangzhou 310027, China*

²*Key Laboratory of Materials Modification by Laser, Ion and Electron Beams, Ministry of Education, Dalian University of Technology, Dalian 116024, China*

³*Department of Materials Science and Engineering & Key Laboratory of 3D Micro/Nano Fabrication and Characterization of Zhejiang Province, Westlake University, Hangzhou 310030, China*

⁴*Research Institute of Core Technology for Materials Innovation, National Institute of Advanced Industrial Science and Technology (AIST), Tsukuba 305-8565, Japan*

⁵*SANKEN (The Institute of Scientific and Industrial Research), Osaka University, 8-1 Mihogaoka, Ibaraki, Osaka 567-0047, Japan*

⁶*Center of Electron Microscopy, State Key Laboratory of Silicon and Advanced Semiconductor Materials, School of Materials Science and Engineering, Zhejiang University, Hangzhou 310027, China*

⁷*College of Chemistry and Molecular Engineering, Peking University, Beijing 100871, China*

⁸*Center for Advanced Optoelectronic Materials, College of Materials and Environmental Engineering, Hangzhou Dianzi University, Hangzhou 310018, China*

⁹*Suzhou Laboratory, Suzhou, 215123, China*

¹⁰*Department of Mechanical Engineering, The University of Tokyo, Tokyo 113-8656, Japan*

[†]*These authors contributed equally*

* Corresponding authors: liwenbin@westlake.edu.cn; gaojf@dlut.edu.cn; suenaga-kazu@sanken.osaka-u.ac.jp; xiangrong@zju.edu.cn

In this work, we present the synthesis of tin disulfide (SnS_2) nanotubes (NTs) with preferred chiral angle. A sacrificial template is used to create channels of boron nitride nanotubes (BNNTs) with an optimized diameter of 4-5 nm, inside of which SnS_2 NTs are formed with the high yield and structural purity. Atomic resolution imaging and nano-area electron diffraction reveal that these synthesized SnS_2 NTs prefer to have an armchair configuration with a probability of approximately 85%. Calculations using density functional theory (DFT) reveal a negligible difference in the formation energy between armchair and zigzag NTs, suggesting that structural stability does not play a key role in this chirality-selective growth. However, a detailed TEM investigation revealed that some SnS_2 nanoribbons are found connected to the ends of SnS_2 NTs, and that these nanoribbons primarily have a zigzag configuration. Subsequent DFT and machine learning potential molecular dynamic simulations verify that nanoribbons with zigzag configurations are more stable than armchair ones, and indeed zigzag nanoribbons aligned along the BNNT axis tend to roll up to form an armchair SnS_2 NTs. Finally, this “zigzag nanoribbon to armchair nanotube” transition hypothesis is verified by *in-situ* high-resolution transmission electron microscopy, in which the transformation of SnS_2 nanoribbons into a nanotube is reproduced in real time. This work is the first demonstration of preferred-chirality growth of transition metal dichalcogenide nanotubes.

One-dimensional (1D) nanotubes exhibit extraordinary quantum phenomena such as 1D confinement and van Hove singularities, resulting in unique mechanical, optical, and electronic properties (1–4). Compared to the well-studied carbon nanotube (CNT), transition metal dichalcogenide nanotubes (TMD NTs) possess a large variety of possible material compositions, providing additional freedom for tuning various material properties from bandgap engineering to exciton–polariton interactions (2, 5–9). In addition, unlike graphene, the TMD lattice is less symmetric, giving rise to a stronger nonlinearity. This has been demonstrated recently in several 1D TMD structures (10–13), but controlling TMD nanotubes’ atomic structure, particularly their chirality (the “twist” of the rolled sheet), remains a fundamental challenge (14, 15). It took more than two decades after the discovery of CNTs to achieve selective growth of specific chiralities, (16–18), whereas there have been very few attempts at chirality-selective growth of TMD NTs three decades after their discovery, and no reliable strategy has been proposed thus far (15, 19, 20). In this work, we synthesized SnS₂ NTs using a tailored CVD technique and achieved preferential synthesis of armchair-configuration at an enrichment of 85%. This claim is supported by numerous sophisticated characterization methods, and the underlying formation mechanism is explained and verified by multiple computational approaches as well as *in situ* transmission electron microscopy.

To produce SnS₂ NTs, we developed a four-step synthesis process schematically illustrated in Fig. 1A. First, single-walled carbon nanotubes (SWCNTs) were utilized as the starting material and sacrificial template. Next, boron nitride nanotubes (BNNT) were formed on the outer surface of the SWCNTs using our original CVD technique, the details of which are described elsewhere (21, 22). Subsequent oxidization in air leaves behind pristine BNNTs with inner diameters of 1–13 nm. Finally, SnS₂ NTs were grown within the BNNT inner channels using KI as a promoter (see Fig. S1 and **SI methods section** for more experimental details). In this growth process, the diameter of the inner channel is pre-determined by the initial SWCNTs, and plays a key role in the successful formation of SnS₂ NTs by forming an efficient reaction space that is neither too small nor too large for producing nanotubes (details shown later). This is the reason why other BNNTs (e.g., commercial products), which typically have a smaller inner diameter, do not result in successful growth (Fig. S2).

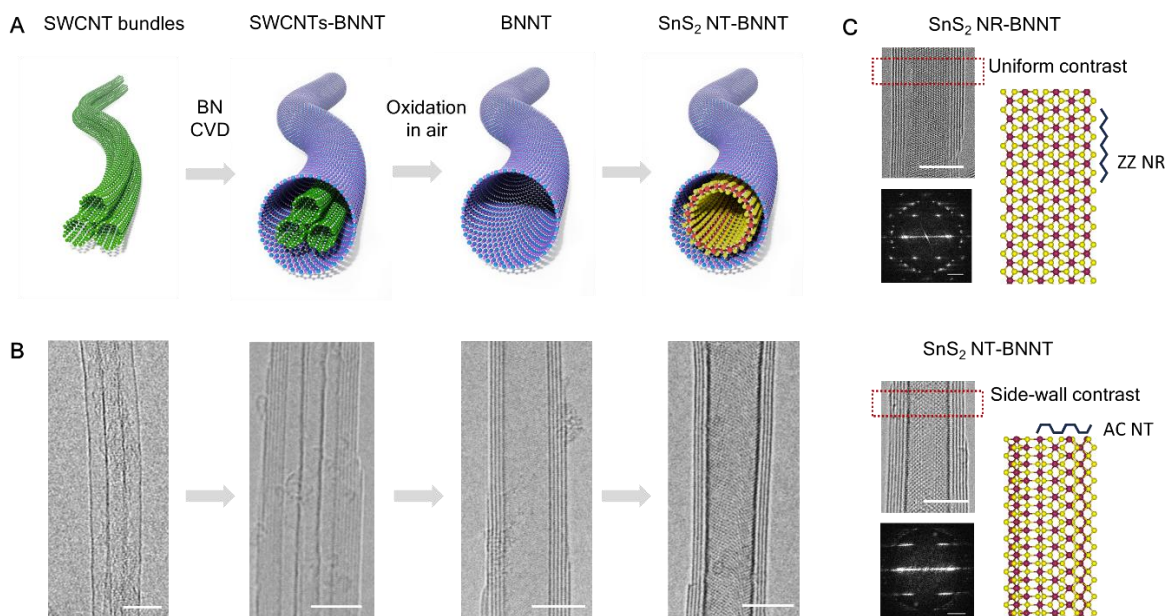


Fig. 1. Synthesis process and structure of SnS₂ NR/NT within BNNT. (A) An atomic model. (B) HR-TEM images present the stepwise synthesis of a SnS₂ NT within a BNNT. (C) HR-TEM images demonstrate the successful synthesis of SnS₂ nanostructures (NR and NT) within BNNTs, and the FFT shows that the NR is zigzag while the NT is armchair. All scale bars are 5 nm.

Figure 1B shows high-resolution transmission electron microscopy (HR-TEM) images of the samples at different growth stages, with BNNT-encapsulated single-walled SnS₂ NTs as a final product. In representative TEM images (Figs. 1B and 1C), SnS₂ NTs inside the BNNTs show a strong contrast at side walls, which is a distinguishing feature of tubular crystals. Nanoribbons are occasionally found inside the BNNTs, and can be differentiated from NTs because they generally exhibit uniform contrast along the entire plane (Fig. 1C). The combination of these features allows one to easily distinguish NTs from nanoribbons in TEM images. Moreover, the diffraction pattern of a ribbon is a group of spaced dots, but these dots blend into prolonged dashed lines in the case of a NT due to the large curvature of the crystal basal plane. Figure 1C also shows the crystal structure and chiral definition of SnS₂ NRs and NTs. In nanoribbons, chirality is conventionally defined following the atomic arrangement of the longer side, whereas for nanotubes, chirality is defined by the atomic arrangement of the edge perpendicular to the axis.

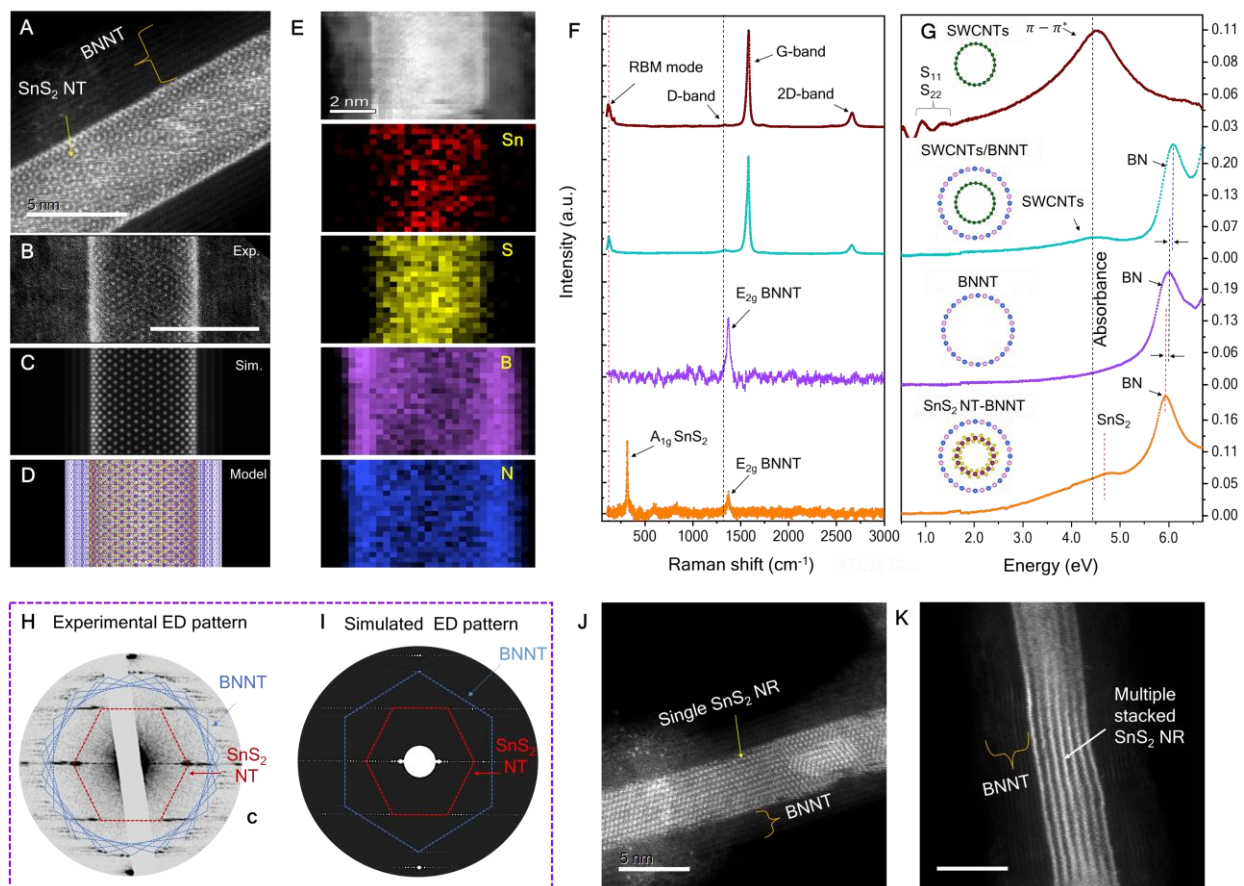


Fig. 2. Comprehensive microscopic and spectroscopic analysis of SnS₂ within BNNT. (A) A HAADF-STEM image of an individual SnS₂ nanotube synthesized inside a BNNT, showing the overall morphology and structural crystallinity. (B) Atomically resolved experimental STEM image of SnS₂ NT within a BNNT. (C) Simulated STEM image supporting the experimental synthesis, and (D) a corresponding atomic model depicts the atomic arrangement of SnS₂ NT within the BNNT. (E) EELS mapping of the marked region shows the elemental distribution of Sn, S, B, and N. (F and G) Raman and UV-vis spectra taken at each growth step that includes SWCNT, SWCNT-BNNT, BNNT, and SnS₂-BNNT. Insets represent atomic models at each stage of SnS₂ NT synthesis, highlighting the distinct structural configurations. (H and I) Experimental and simulated NAED patterns from a region containing SnS₂ NT inside BNNT. (J and K) STEM images showing the diverse structural integrity of SnS₂ nanostructures (single NR, and multiple stacked NR) encapsulated within BNNTs.

Figure 2 comprehensively characterizes the structural, elemental, and optical properties of SnS₂ NTs using various spectroscopic and microscopic techniques. Figure 2A presents a STEM-

HAADF image showing the atomic arrangement of the SnS₂ NT. Hollow SnS₂ NTs are clearly encapsulated within each BNNT. This crystalline arrangement reveals the highly ordered 1T phase atomic structure (23, 24), but the atomic structure can differ slightly depending on the chiral angle of these NTs. For example, in a chiral NT, strong Moiré patterns are generated by the different contrast of the top and bottom tube walls (Fig. 2A and Fig. S3), but in an achiral NT, this effect is weak (Fig. 2B). Figure 2B compares the experimental HAADF image with the simulated image (Fig. 2C, and atomic model in Fig. 2D) from a 1T SnS₂ NT with chiral index of (22,22). These images show a high degree of consistency, confirming that structurally complete and single-crystal SnS₂ NT is obtained. Elemental mapping using electron energy-loss spectroscopy (EELS) shown in Fig. 2E displays the spatial distribution of Sn, S, B, and N throughout the region. The heterostructure contains Sn (red) and S (yellow) signals that are restricted to the BNNT inner channel, while B (magenta) and N (blue) signals appear distributed across the heterostructure from the BNNT front, back, and sidewalls. Additional STEM images and EDS mapping of the SnS₂ reveal that we obtained NTs with diameters ranging from 1 to 7 nm (Fig. S4 and S5).

The chemical nature of the SnS₂ NTs was characterized by Raman scattering and optical absorption spectroscopy (Fig. 2F, 2G and Fig. S6). Raman spectra of the sample at different stages, e.g. SWCNT, SWCNT-BNNT, BNNT, and SnS₂-BNNT, exhibit distinct features. SWCNTs show dominant G- and 2D-bands and radial breathing mode (RBM) peaks, whereas BNNTs show a single E_{2g} mode at 1369 cm⁻¹ (21, 25). In the final product, only the A_{1g} mode of SnS₂ at 314 cm⁻¹ becomes dominant, confirming the successful formation of a heterostructure containing SnS₂ within a BNNT (26, 27). The peak at 314 cm⁻¹ also distinguishes 1T SnS₂ from possibly the other common composition of Sn and S, e.g., SnS, as it has multiple peaks from 50-250 cm⁻¹ (28). UV-vis absorption spectra were measured at different synthesis steps (Fig. 2G). The evolution of absorption peaks agrees with Raman spectra and confirms the successful encapsulation of SnS₂ within BNNTs, with well-defined chemical states and bonding environments for all elements.

Electron diffraction is a powerful tool and precisely describes the atomic periodicity of a crystal by elastic scattering (29–32). Figure 2H presents the nano area electron diffraction (NAED) pattern from a SnS₂ NT encapsulated in a BNNT. The diffraction pattern exhibits contributions from both materials: the SnS₂ reflections are highlighted with red hexagons while the BNNT reflections are shown with a group of blue hexagons. We first note that all patterns are prolonged dashed lines

rather than regularly spaced dots, confirming curvature of the atomic sheets in SnS₂ NTs and BNNTs. Secondly, the alignment of the hexagons describes the chiral angle of the NTs. The apparently random orientation of blue hexagons suggests that the outer BNNTs have no preferred chiral angle, however the singular inner red hexagon clearly reveals that the measured SnS₂ NTs exhibit a well-defined armchair chirality (discussion continues later). We also performed simulations of NAED patterns to further validate the experimental observations. The simulated patterns of a single-walled SnS₂ NT inside a single-walled BNNT (Fig. 2I) demonstrate excellent agreement with the experimental ED pattern, thus confirming the structural character. Figures 2J, and 2K reveal less-common products, such as single-layer NR and multi-layer (stacked) NR within the BNNTs, through HAADF-STEM images (more details in Fig. S7). Note once again that NTs and NRs show clear differences in HAADF images.

Figure 3 demonstrates an extensive evaluation of the chirality distribution of SnS₂ NTs formed inside BNNT templates. Very few studies have addressed the chirality of TMD NTs, possibly due to the limited availability of samples, particularly single-walled nanotubes. Figure 3A displays a probability distribution graph that quantifies the statistical prevalence of different chirality types in SnS₂ NTs. Figure 3(B, E, and H and S8) presents HR-TEM images of the SnS₂ NT-BNNT heterostructure, focusing on the nanobeam regions. Correspondingly, Fig. 3(C, F, and I) showcases the NAED patterns obtained from the respective tubes. The diffraction patterns exhibit six-fold symmetry, characteristic of SnS₂ NTs, and corresponding to three distinct configurations: AC ($n = m$), near-ZZ (n or $m = 0$), and chiral ($n \neq m$) (33). Figure 3 (D, G, and J) presents the atomic structure of SnS₂ NTs in these three configurations. We established statistical confidence by studying more than 60 NAED patterns that included 40 NTs and 20 NRs, with additional data presented in Fig. S9. Figures 3L, and 3M provide atomic models, simulated NAED, and additional experimental NAED patterns for SnS₂ NRs and NTs. Notably, out of 40 SnS₂ NTs, 34 exhibited AC structure, while four were near-ZZ and only two were chiral. The analysis demonstrates a strong preference for SnS₂ NTs to adopt armchair chirality with an approximate probability of 85%. For comparison, within the very few attempts found in literature, An et al. confirmed that different shells in multiwalled WS₂ NTs tend to have a uniform chiral angle within a single tube, and Nakanishi et al. found that the chirality of MoS₂ NTs are random (14, 34). Meanwhile, all 20 SnS₂ NRs coexisting here displayed ZZ configurations (Fig. S10, and reason to discuss later).

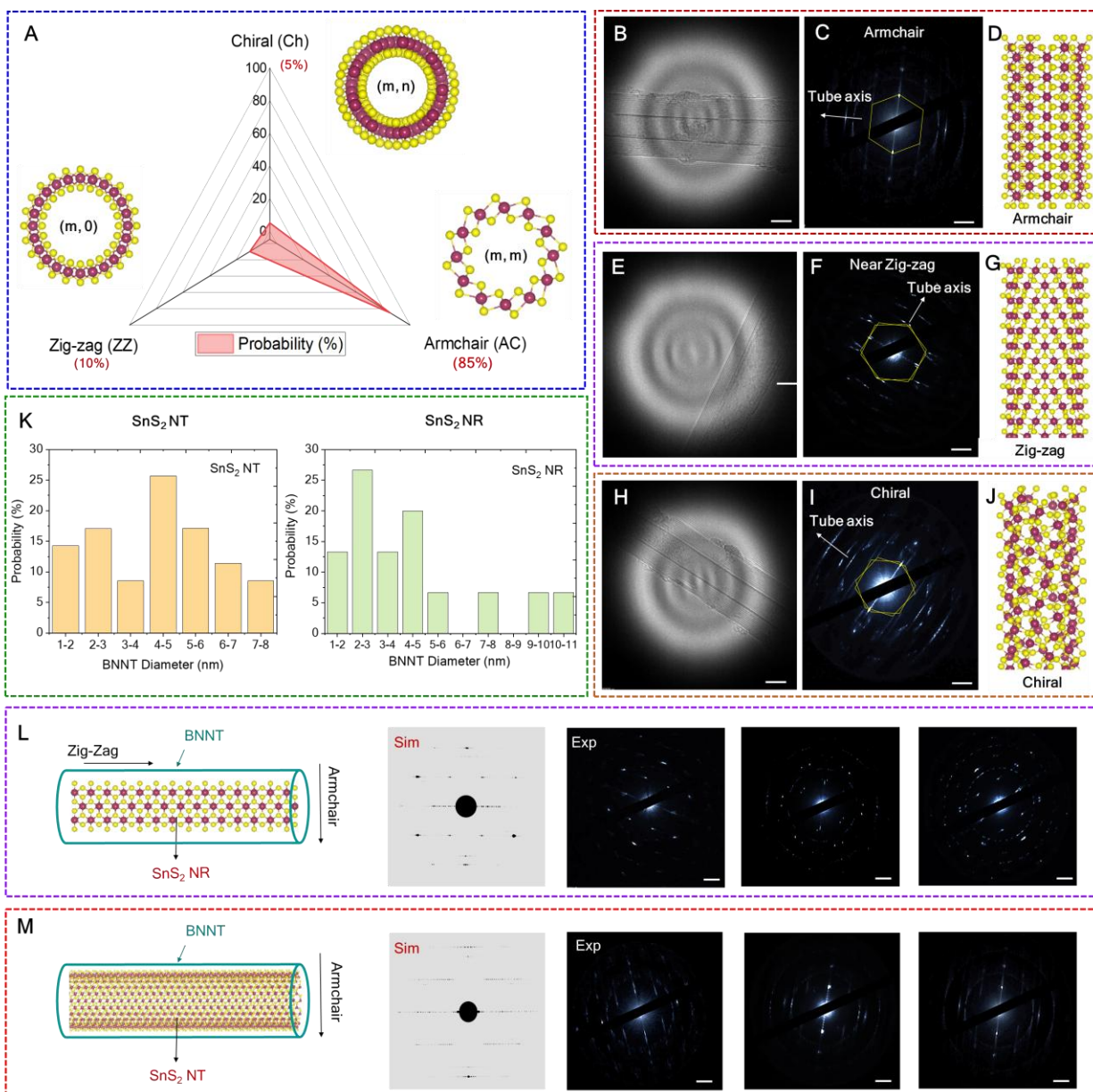


Fig. 3. Chirality distribution for SnS₂ NTs and NRs (A) A radar plot illustrates the distributions of various chirality types of SnS₂ NTs formed within the host nanotubes. Panels (B), (E), and (H) display nano-area beam HR-TEM images of SnS₂ NTs within BNNTs. Panels (C), (F), and (I) show corresponding NAED images of the NTs, while panels (D), (G), and (J) provide atomic models of armchair, near-zigzag, and chiral SnS₂ NTs (K) Probability distributions of SnS₂ nanostructures—namely nanotubes (NT) and nanoribbons (NR)—formed inside the host, as a function of the host's diameter. (L and M) atomic models, and NAED patterns (simulated and experimental) of SnS₂ NR and NT inside the host tube.

The distribution probability of different morphologies of SnS₂ inside BNNT as a function of host diameter is presented by the bar graph shown in Fig. 3K. The two panels represent distinct nanostructures, with light gold representing the NTs and tea green representing NRs. The y-axis shows the probability (%) of occurrence, while the x-axis represents the BNNT diameter in nanometers. For SnS₂ NTs, the maximum probability of formation occurs within BNNTs with diameters of 4-6 nm, suggesting that larger diameters favor the growth of NTs, whereas SnS₂ NR formation reaches its peak when BNNTs have smaller diameters (2-5 nm), since these tighter constraints help maintain ribbon-like morphologies.

To understand the origin of the AC chirality preference of SnS₂ NT, we investigate the stability of AC and ZZ configurations (the atomic structures shown in Fig. 4A) using DFT simulations. Fig. 4B shows the formation energies of AC and ZZ SnS₂ NTs normalized to that of SnS₂ monolayer as a function of radius. Interestingly, the formation energy of AC and ZZ SnS₂ NTs with similar radii are nearly identical, implying the armchair structure is not more energetically favorable than the zigzag structure in SnS₂ NTs. Since the intrinsic NT stability alone cannot explain the experimentally observed chirality selection, we examined the energetics of SnS₂ NRs, which are sometimes found attached to the end of SnS₂ NTs (Fig. S11). The energy per unit length of SnS₂ NRs depends on their width, and comparisons between the ZZ and AC configurations are revealed in Fig. 4C. The ZZ configuration exhibits a clear and consistent lower formation energy than the AC configuration by ~1.0 eV/nm. By analyzing the formation of NRs from monolayer with bonding breaking and coordination number change, it provides a clear rationale for the observed energy differences between different NRs. For ZZ NR formation from the monolayer, two dangling bonds per unit length are formed along the ribbon edges, resulting from the cleavage of two Sn-S bonds. The coordination number of the edge Sn atoms is 5. In contrast, forming AC NR contains approximately $4/\sqrt{3}$ dangling bonds per unit length and the Sn coordination number of edge is 4. This indicates that forming AC NRs requires breaking more bonds and induces a greater reduction in coordination, resulting in higher energy difference relative to ZNR formation. Thus, ZZ NRs are more energetically stable than AC NRs. (Fig. 4A and Table S1). This perfectly explains our observation about NR in Fig. 3, where all (20 out of 20) NRs were found to be zigzag. Besides, we used DFT calculations of the SnS₂ NR-BNNT system (Fig. 4D) to further investigate the adhesion energy between ZZ SnS₂ NRs and BNNTs. The adhesive interaction not only

stabilizes the SnS₂ NR but also can cause deformation to BNNT template, which is later observed both in experiments and simulations.

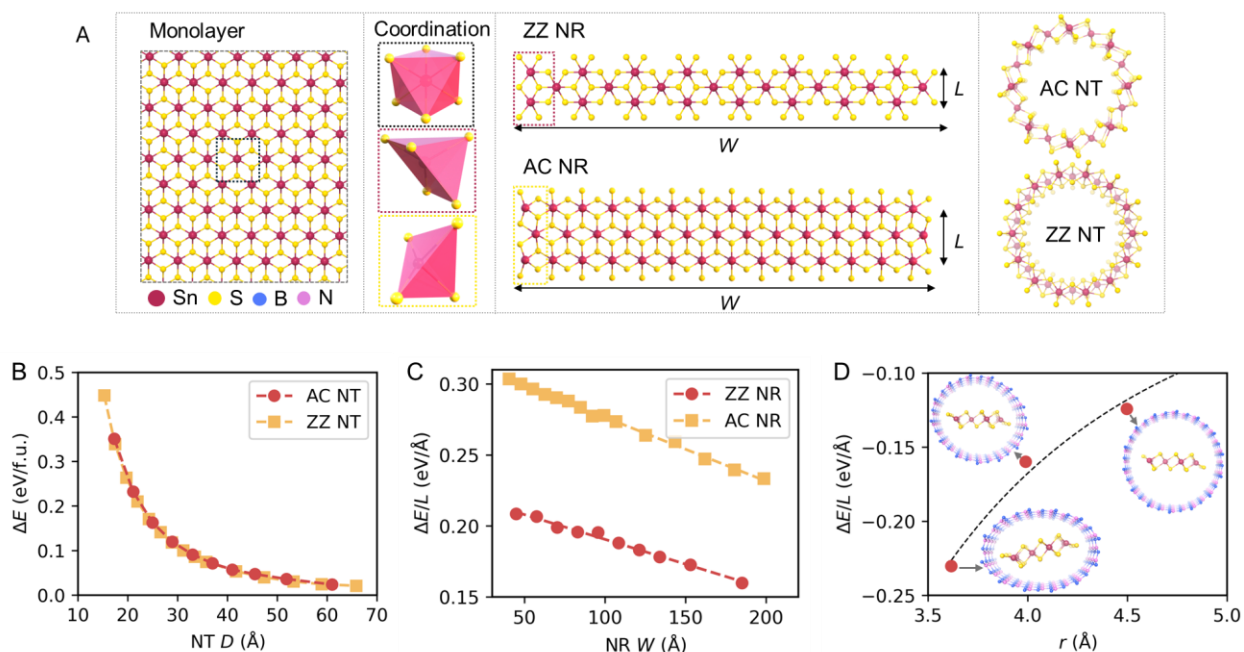


Fig. 4. Schematic illustration of DFT energy calculations for SnS₂ NR and NT. (A) The formation of SnS₂ nanotube from monolayer. The orders of subplots in (A) are SnS₂ monolayer, the coordination number of Sn in monolayer and NR's edge, the SnS₂ NRs, and the SnS₂ NTs. The dashed square in monolayer and NRs are corresponding to the coordination numbers with the same color squares. Zigzag SnS₂ NTs rolled from armchair NRs, and armchair SnS₂ NTs rolled from zigzag NRs. "Coord." represents coordination number. (B) Normalized energy of SnS₂ NTs as a function of NT diameter. The NT energy was normalized to the energy of the SnS₂ monolayer, and f.u. represents the formula unit of SnS₂. NR and NT represent nanoribbons and nanotubes, respectively. "ZZ" and "AC" denote zigzag and armchair, respectively. (C) Normalized energy of NRs to the width (W) of the NRs. The y-axis shows the normalized energy of NRs to that of SnS₂ monolayer per length ($1/L$) in the periodic direction. (D) Adhesion energy per edge length calculated for SnS₂ NR to the BNNT as a function of the distance between the edge of the NR and the wall of the BNNT. The SnS₂ NR chiral index is (2, 2). The three BNNT chiral index are (12, 12), (13, 13), (14, 14), respectively. The atomic structures of BNNT@SnS₂NR are included in (D). The structural detail is summarized in Table S2.

After confirming that ZZ NRs are significantly more stable and observing that some NRs are connected to SnS₂ NTs, it is reasonable to speculate that AC SnS₂ NTs may have been formed via a transition from ZZ NRs. To elucidate this mechanism, we carried out MD calculations, additional HAADF observations and simulations, and *real-time* TEM experiments to trace this possible transformation from SnS₂ NRs to NTs. We developed a machine learning potential (MLP) using DFT data with details shown in figs. S12-14. This technique demonstrates excellent predictive accuracy when measuring system energetics by mean absolute errors reaching 12 meV/atom and 182 meV/Å. The close agreement between DFT and MLP results supports the validity of using MLP for large-scale simulations of SnS₂ nanostructures. We dynamically simulate the transition process from three-layer SnS₂ NRs to a NT confined within a BNNT. The MLP MD simulations (movie S1 and Fig. S15-17) show SnS₂ nanoribbons are layered peeled off by the h-BN layers and then slip along h-BN inner wall during vibrations. The two ZZ edges of separate SnS₂ ribbons have a chance to close each other and connect into a curved wide SnS₂ nanoribbon to release the edge energy, which eventually leads to the transformation of SnS₂ nanoribbons into nanotubes.

Details of this process are further simulated using MLP MD with over 100K atoms (Fig 5A, and Movie S2, S3). The transformation can be divided into several key steps. First, the interaction of the multilayer NR with the BNNT induces pronounced local distortions. Next, the conversion initiates at one end of the NR: the two outermost ribbons merge into a single layer, local strain drives the cross-section toward circularity, and an intermediate structure emerges. As the process proceeds, the outer ribbons fully coalesce, whereupon the inner ribbon begins to slide, yielding another metastable configuration. Finally, the accumulated strain and interlayer sliding complete the conversion of the three-layer NR into the NT geometry. Simulated STEM images of these key transient atomic structures were compared with experimental STEM images collected in the real sample. Strikingly similar morphologies are indeed identified in simulated (Fig. 5B) and experimentally obtained STEM images (Fig. 5C.) This excellent agreement demonstrates that the model accurately reproduces the experimentally observed structural features and deformation modes.

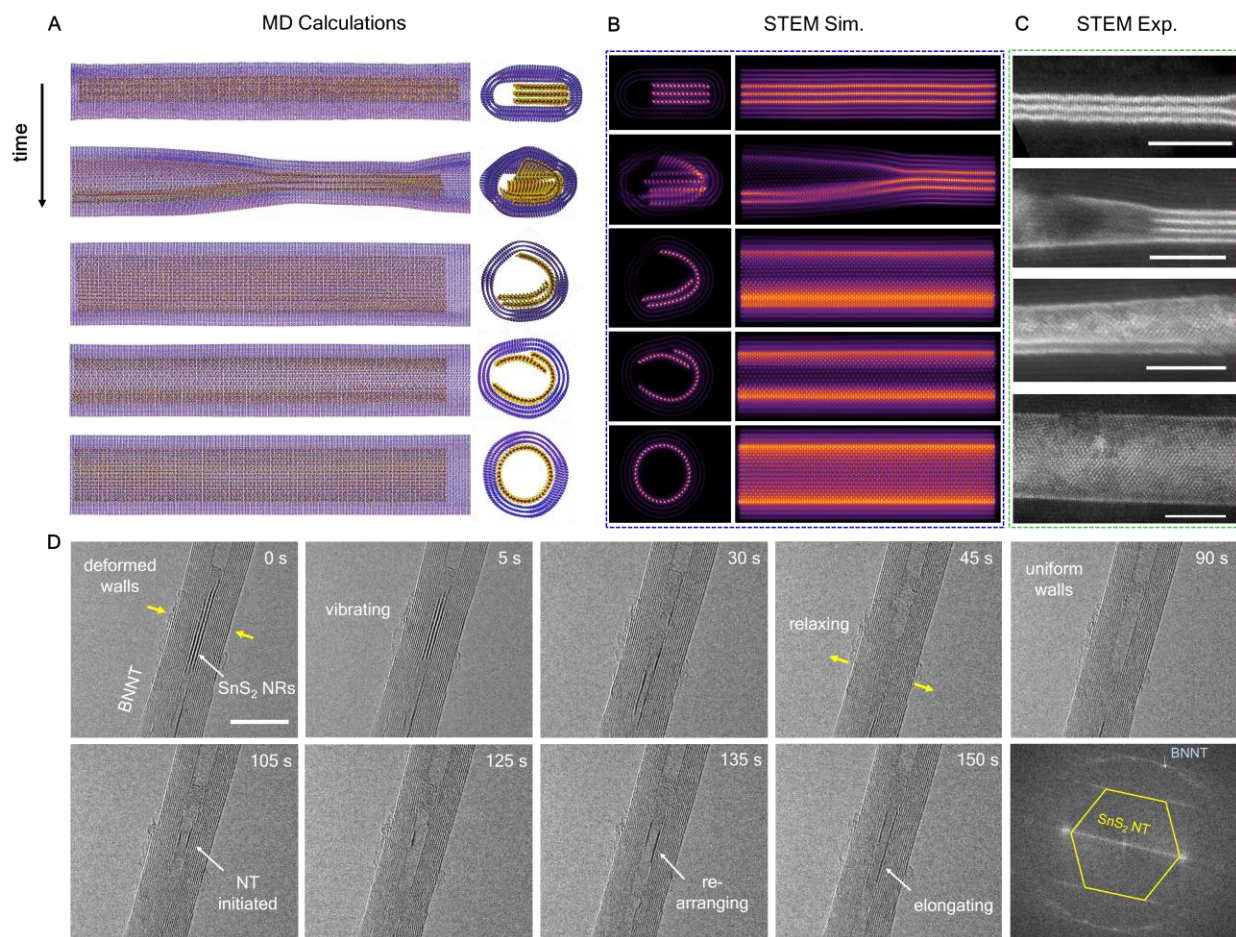


Fig. 5. In situ structural evolution from SnS₂ NR to NT and the associated deformation induced by interactions with a BNNT. (A) The atomic models, (B) simulated STEM images corresponding to the respective atomic models, and (C) experimentally acquired STEM images illustrate the transformation pathway. The simulated STEM images closely match the experimental STEM observations, confirming the validity of the proposed transformation mechanism. Scale bar 5 nm. (D) HR-TEM image illustrating the broad overview of the transformation from SnS₂ NRs into NT under electron beam irradiation operated at 200 kV, and FFT showing the armchair chirality of the finally transformed nanotube. All scale bar 10 nm.

Finally, the MD simulated transformation process is observed in real-time by *in situ* TEM. Figure 5D presents HR-TEM snapshots captured at various stages of the transformation process, (movie S4 for the entire process). An electron beam with 200 kV and 8200 e/Å²/s was utilized to mimic the energy input at high temperatures. The atomic structure of SnS₂ transforms naturally into a more energetically stable curved configuration. The surrounding BNNT offers structural stability that facilitates the transformation from a flat ribbon geometry into a cylindrical nanotube

shape. When the curvature reaches a critical threshold, the edges of the SnS₂ NRs begin to connect, leading to the closure of the nanotube structure. The FFT of the final NT confirm its armchair structure, as detailed in Fig. 5D. These observations provide direct evidence of the structural evolution from ZZ NRs to AC NTs, supported by thermodynamic and kinetic factors governing the transformation. Notably, there is an observable deformation of the BNNT channel in the first frame (0 s), and this deformation is released at a later frame (65 s), which fully reproduces the simulated process shown in Fig. 5A.

We have demonstrated a preferred synthesis armchair SnS₂ nanotubes happened within BN nanotube templates. DFT, machine learning potential MD calculations, comparison of simulated and experimental HAADF-STEM images, and *in-situ* real-time HR-TEM observations have provided a consistent and robust explanation to the structural selectivity. This work provides us with a solution to the three-decades-pending issue, and may inspire the controlled synthesis of other types of nanotubes, bringing new possibilities for investigating not only fundamental science but also potential applications of 1D van der Waals crystals.

References

1. S. Iijima, Helical microtubules of graphitic carbon. *Nature* **354**, 56–58 (1991).
2. R. Tenne, L. Margulis, M. Genut, G. Hodes, Polyhedral and cylindrical structures of tungsten disulphide. *Nature* **360**, 444–446 (1992).
3. N. G. Chopra, R. J. Luyken, K. Cherrey, V. H. Crespi, M. L. Cohen, S. G. Louie, A. Zettl, Boron Nitride Nanotubes. *Science (1979)* **269**, 966–967 (1995).
4. S. M. Bachilo, M. S. Strano, C. Kittrell, R. H. Hauge, R. E. Smalley, R. B. Weisman, Structure-Assigned Optical Spectra of Single-Walled Carbon Nanotubes. *Science* **298**, 2361–2366 (2002).
5. Q. Qian, R. Zu, Q. Ji, G. S. Jung, K. Zhang, Y. Zhang, M. J. Buehler, J. Kong, V. Gopalan, S. Huang, Chirality-Dependent Second Harmonic Generation of MoS₂ Nanoscroll with Enhanced Efficiency. *ACS Nano* **14**, 13333–13342 (2020).
6. S. S. Sinha, A. Zak, R. Rosentsveig, I. Pinkas, R. Tenne, L. Yadgarov, Size-Dependent Control of Exciton–Polariton Interactions in WS₂ Nanotubes. *Small* **16**, 1904390 (2020).
7. Y. Chen, S. Qian, K. Wang, X. Xing, A. Wee, K. P. Loh, B. Wang, D. Wu, J. Chu, A. Alu, P. Lu, C.-W. Qiu, Chirality-dependent unidirectional routing of WS₂ valley photons in a nanocircuit. *Nat Nanotechnol* **17**, 1178–1182 (2022).
8. B. Xiang, R. Wang, Y. Chen, Y. Wang, T. Qin, M. Zhang, K. Watanabe, T. Taniguchi, W. Duan, P. Tang, H. Liu, Q. Xiong, Chirality-Dependent Dynamic Evolution for Trions in Monolayer WS₂. *Nano Lett* **24**, 6592–6600 (2024).
9. L. Yadgarov, R. Tenne, Nanotubes from Transition Metal Dichalcogenides: Recent Progress in the Synthesis, Characterization and Electrooptical Properties. *Small* **n/a**, 2400503 (2024).
10. Y. J. Zhang, T. Ideue, M. Onga, F. Qin, R. Suzuki, A. Zak, R. Tenne, J. H. Smet, Y. Iwasa, Enhanced intrinsic photovoltaic effect in tungsten disulfide nanotubes. *Nature* **570**, 349–353 (2019).
11. G. Xue, Z. Zhou, Q. Guo, Y. Zuo, W. Wei, J. Yang, P. Yin, S. Zhang, D. Zhong, Y. You, X. Sui, C. Liu, M. Wu, H. Hong, Z.-J. Wang, P. Gao, Q. Li, L. Zhang, D. Yu, F. Ding, Z. Wei, C. Liu, K. Liu, WS₂ ribbon arrays with defined chirality and coherent polarity. *Science* **384**, 1100–1104 (2024).
12. C. Ma, C. Ma, C. Liu, Q. Guo, C. Huang, G. Yao, M. Li, J. Qi, B. Qin, X. Sui, J. Li, M. Wu, P. Gao, W. Wang, X. Bai, Z. Sun, E. Wang, H. Hong, K. Liu, *Nature Nanotechnology* **19**, 1299–1305 (2024).
13. B. Qin, C. Ma, Q., X. Li, W. Wei, C. Ma, Q. Wang, F. Liu, M. Zhao, G. Xue, J. Qi, M. Wu, H. Hong, L. Du, Q. Zhao, P. Gao, X. Wang, E. Wang, G. Zhang, C. Liu, K. Liu. Interfacial epitaxy of multilayer rhombohedral transition-metal dichalcogenide single crystals. *Science* **385**, 99–104 (2024).
14. Q. An, W. Xiong, F. Hu, Y. Yu, P. Lv, S. Hu, X. Gan, X. He, J. Zhao, S. Yuan, Direct growth of single-chiral-angle tungsten disulfide nanotubes using gold nanoparticle catalysts. *Nat Mater* **23**, 347–355 (2024).
15. F. Qin, W. Shi, T. Ideue, M. Yoshida, A. Zak, R. Tenne, T. Kikitsu, D. Inoue, D. Hashizume, Y. Iwasa, Superconductivity in a chiral nanotube. *Nat Commun* **8**, 14465 (2017).
16. F. Yang, X. Wang, D. Zhang, J. Yang, D. Luo, Z. Xu, J. Wei, J.-Q. Wang, Z. Xu, F. Peng, X. Li, R. Li, Y. Li, M. Li, X. Bai, F. Ding, Y. Li, Chirality-specific growth of single-walled carbon nanotubes on solid alloy catalysts. *Nature* **510**, 522–524 (2014).

17. S. Zhang, L. Kang, X. Wang, L. Tong, L. Yang, Z. Wang, K. Qi, S. Deng, Q. Li, X. Bai, F. Ding, J. Zhang, Arrays of horizontal carbon nanotubes of controlled chirality grown using designed catalysts. *Nature* **543**, 234–238 (2017).
18. Z. Zhang, Y. Chen, P. Shen, J. Chen, S. Wang, B. Wang, S. Ma, B. Lyu, X. Zhou, S. Lou, Z. Wu, Y. Xie, C. Zhang, L. Wang, K. Xu, H. Li, G. Wang, K. Watanabe, T. Taniguchi, D. Qian, J. Jia, Q. Liang, X. Wang, W. Yang, G. Zhang, C. Jin, W. Ouyang, Z. Shi, Homochiral carbon nanotube van der Waals crystals. *Science (1979)* **387**, 1310–1316 (2025).
19. M. Remškar, Z. Škraba, P. Stadelmann, F. Lévy, Structural Stabilization of New Compounds: MoS₂ and WS₂ Micro- and Nanotubes Alloyed with Gold and Silver. *Advanced Materials* **12**, 814–818 (2000).
20. M. Bar-Saden, R. Tenne, The gold ticket to achiral WS₂ nanotubes. *Nat Mater* **23**, 310–311 (2024).
21. R. Xiang, T. Inoue, Y. Zheng, A. Kumamoto, Y. Qian, Y. Sato, M. Liu, D. Tang, D. Gokhale, J. Guo, K. Hisama, S. Yotsumoto, T. Ogamoto, H. Arai, Y. Kobayashi, H. Zhang, B. Hou, A. Anisimov, M. Maruyama, Y. Miyata, S. Okada, S. Chiashi, Y. Li, J. Kong, E. I. Kauppinen, Y. Ikuhara, K. Suenaga, S. Maruyama, One-dimensional van der Waals heterostructures. *Science (1979)* **367**, 537–542 (2020).
22. Y. Zheng, A. Kumamoto, K. Hisama, K. Otsuka, G. Wickerson, Y. Sato, M. Liu, T. Inoue, S. Chiashi, D.-M. Tang, Q. Zhang, A. Anisimov, E. I. Kauppinen, Y. Li, K. Suenaga, Y. Ikuhara, S. Maruyama, R. Xiang, One-dimensional van der Waals heterostructures: Growth mechanism and handedness correlation revealed by nondestructive TEM. *Proceedings of the National Academy of Sciences* **118**, e2107295118 (2021).
23. J. Xu, S. Lai, M. Hu, S. Ge, R. Xie, F. Li, D. Hua, H. Xu, H. Zhou, R. Wu, J. Fu, Y. Qiu, J. He, C. Li, H. Liu, Y. Liu, J. Sun, X. Liu, J. Luo, Semimetal 1H-SnS₂ Enables High-Efficiency Electroreduction of CO₂ to CO. *Small Methods* **4**, 2000567 (2020).
24. Z. Ma, Z. Yao, Y. Cheng, X. Zhang, B. Guo, Y. Lyu, P. Wang, Q. Li, H. Wang, A. Nie, A. Aspuru-Guzik, All roads lead to Rome: Sodiation of different-stacked SnS₂. *Nano Energy* **67**, 104276 (2020).
25. S. Wang, D. I. Levshov, K. Otsuka, B.-W. Zhang, Y. Zheng, Y. Feng, M. Liu, E. I. Kauppinen, R. Xiang, S. Chiashi, W. Wenseleers, S. Cambré, S. Maruyama, Evaluating the Efficiency of Boron Nitride Coating in Single-Walled Carbon-Nanotube-Based 1D Heterostructure Films by Optical Spectroscopy. *ACS Nano* **18**, 9917–9928 (2024).
26. B. Li, T. Xing, M. Zhong, L. Huang, N. Lei, J. Zhang, J. Li, Z. Wei, A two-dimensional Fe-doped SnS₂ magnetic semiconductor. *Nat Commun* **8**, 1958 (2017).
27. Y. Gong, H. Yuan, C.-L. Wu, P. Tang, S.-Z. Yang, A. Yang, G. Li, B. Liu, J. van de Groep, M. L. Brongersma, M. F. Chisholm, S.-C. Zhang, W. Zhou, Y. Cui, Spatially controlled doping of two-dimensional SnS₂ through intercalation for electronics. *Nat Nanotechnol* **13**, 294–299 (2018).
28. M. Li, Y. Wu, T. Li, Y. Chen, H. Ding, Y. Lin, N. Pan, X. Wang, Revealing anisotropy and thickness dependence of Raman spectra for SnS flakes. *RSC Adv* **7**, 48759–48765 (2017).
29. L. MARGULIS, P. DLUZEWSKI, Y. FELDMAN, R. TENNE, TEM study of chirality in MoS₂ nanotubes. *J Microsc* **181**, 68–71 (1996).
30. S. Amelinckx, A. Lucas, P. Lambin, Electron diffraction and microscopy of nanotubes. *Reports on Progress in Physics* **62**, 1471 (1999).
31. J. M. Zuo, I. Vartanyants, M. Gao, R. Zhang, L. A. Nagahara, Atomic Resolution Imaging of a Carbon Nanotube from Diffraction Intensities. *Science (1979)* **300**, 1419–1421 (2003).
32. Y. Chen, H. Deniz, L.-C. Qin, Accurate measurement of the chirality of WS₂ nanotubes. *Nanoscale* **9**, 7124–7134 (2017).

33. G. Radovsky, R. Popovitz-Biro, R. Tenne, Study of Tubular Structures of the Misfit Layered Compound SnS₂/SnS. *Chemistry of Materials* **24**, 3004–3015 (2012).
34. Y. Nakanishi, S. Furusawa, Y. Sato, T. Tanaka, Y. Yomogida, K. Yanagi, W. Zhang, H. Nakajo, S. Aoki, T. Kato, K. Suenaga, Y. Miyata, Structural Diversity of Single-Walled Transition Metal Dichalcogenide Nanotubes Grown via Template Reaction. *Advanced Materials* **35**, 2306631 (2023).